

Chapter 44

Use of neutron imaging for proton exchange membrane fuel cell (PEMFC) performance analysis and design

**T. A. Trabold¹, J. P. Owejan¹, J. J. Gagliardo¹, D. L. Jacobson²,
D. S. Hussey² and M. Arif²**

¹General Motors Corporation, Honeoye Falls, NY, USA

²National Institute of Standards and Technology (NIST), Gaithersburg, MD, USA

1 INTRODUCTION

Over the last decade, proton exchange membrane fuel cells (PEMFCs) have become the subject of intensive research activity, as the technology offers a viable alternative to power sources based on hydrocarbon combustion. Water management stands out as one of the key remaining performance, durability, and cost challenges, because it influences the properties of the materials used in the membrane-electrode assembly (MEA), gas diffusion layer (GDL), and bipolar plates; drives the selection of fuel cell operating conditions (temperature, pressure, relative humidity, and reactant stoichiometric ratios); and impacts bipolar plate and hardware design as well as specification of ancillary components, such as the air- and hydrogen (or reformat)-handling equipment, humidifiers, etc. In the event that high-temperature, low-humidity proton exchange membranes become viable, there will still be a need to accommodate the presence of liquid water under start-up, shutdown, and transient load conditions, and for low ambient temperature performance. Therefore, a strong and sustained need for diagnostic methods that enable measurement of liquid water within an operating fuel cell is expected.

A variety of methods have been advanced for monitoring the *in situ* liquid water content, as recently summarized

by St. Pierre.^[1] Neutron imaging has several inherent advantages that make it among the most versatile diagnostic methods:

- The high neutron cross section of hydrogen, coupled with the low neutron cross section of common fuel cell construction materials, provides an acceptably high signal-to-noise level without significant deviation from a standard fuel cell design and material set.
- High spatial resolution, on the order of 100 μm or less.
- High temporal resolution, on the order of 10 s or less.
- Large imaging area, on the order of 10 cm \times 10 cm.

More details on the specific experimental features of a typical system for applying neutron imaging to fuel cells are provided in Section 2.

Despite the demonstrated capability of neutron imaging for fuel cell research, the method has a significant disadvantage in that a high-intensity neutron source is needed to attain an acceptable signal-to-noise ratio and image resolution. The cost and radiation safety considerations associated with such a neutron source have limited the number of facilities that possess this unique experimental capability. As of mid-2008, all known publications documenting the application of neutron imaging to PEMFCs^[2–41] have originated from one of seven laboratories (Table 1):

Table 1. Neutron imaging of hydrogen PEMFCs: literature survey 1999 through mid-2008.

Author(s)	Year	NR facility	Active area (cm ²)	Application
Bellows <i>et al.</i> ^[2]	1999	NIST	5	Water gradients in Nafion [®] membranes. Usually cited as the first study of fuel cell water using neutron imaging.
Geiger <i>et al.</i> ^[3]	2002	PSI	100	Flow field water during fuel cell start-up and shutdown. Most water observed on the anode side, as a result of condensation.
Owejan ^[4]	2003	NIST	50	Effects of GDL properties, and channel geometry and surface contact angle on water accumulation.
Satija <i>et al.</i> ^[5]	2004	NIST	?	Demonstration of real-time radiography at 2 s image acquisition intervals, neutron tomography, and masking to isolate anode and cathode flow fields.
Chuang <i>et al.</i> ^[6]	2005	PSU	50	Effect of land and channel widths on voltage loss due to flooding and anode dry out.
Kim <i>et al.</i> ^[7]	2005	NIST	?	Feasibility test to study channel water accumulation at different cell temperatures and current densities.
Kramer <i>et al.</i> ^[8]	2005	PSI	100	Effect of flow field design on water accumulation in channels and GDL.
Pekula <i>et al.</i> ^[9]	2005	PSU	50	Channel-level water quantification as a function of current density.
Schneider <i>et al.</i> ^[10]	2005	PSI	29.2	Simultaneous neutron radiography and locally resolved impedance spectroscopy.
Hickner <i>et al.</i> ^[11]	2006a	NIST	50	Relative responses of current density and hydration state of the fuel cell, the latter being strongly influenced by cell temperature and waste heat.
Hickner <i>et al.</i> ^[12]	2006b/2008	NIST	50	Relative responses of current density and hydration state of the fuel cell, and down-the-channel condensation model.
Hussey <i>et al.</i> ^[13]	2006/2008	NIST	4	Tomographic imaging to distinguish between water accumulation on anode and cathode sides.
Kim <i>et al.</i> ^[14]	2006a	KAERI	100	Channel and MEA/GDL level water during start-up and steady state.
Kim <i>et al.</i> ^[15]	2006b/2008	KAERI	100	Comparison of water management performance of different flow fields, and efficiency of water removal at channel and MEA scales.
Kowal <i>et al.</i> ^[16]	2006	PSU	12.5	Effect of GDL type on water accumulation under channels and lands and under transient and steady-state conditions.
Ludlow <i>et al.</i> ^[17]	2006	NIST	50	Channel and MEA/GDL level water at steady state and after purge.
Manke <i>et al.</i> ^[18]	2006	HMI	Various	Combined neutron imaging with current distribution, and tomographic imaging of various fuel cell stack designs.
Owejan <i>et al.</i> ^[19]	2006a	NIST	50	Water content and differential pressure used to calculate relative permeability in GDL.
Owejan <i>et al.</i> ^[20]	2006b/2008	NIST	50	Bypass loop on cathode used to simulate relationship between voltage instability and water content in a multicell assembly.
Trabold <i>et al.</i> ^[21]	2006	NIST	50	Effects of current density and cathode stoichiometric ratio on channel-level water accumulation.
Turhan <i>et al.</i> ^[22]	2006a	PSU	12.5 and 50	Effects of channel/land width ratio and channel surface energy, and diffusion media type on total water accumulation.

(continued overleaf)

Table 1. (continued).

Author(s)	Year	NR facility	Active area (cm ²)	Application
Turhan <i>et al.</i> ^[23]	2006b	PSU	14.5	Quantify liquid water in channels and diffusion media as a function of inlet gas flow rate and humidification, and cell pressure.
Turhan <i>et al.</i> ^[24]	2006c	PSU	12.5 and 50	Effects of channel/land width ratio and channel surface energy, and diffusion media type on total water accumulation.
Ueda <i>et al.</i> ^[25]	2006/2008	JAERI/KURRI	?	Effect on cell performance of water condensation on anode and cathode sides.
Yoshizawa <i>et al.</i> ^[26]	2006	PSI	127	Effects of diffusion media type and flow field design on quantity of total accumulated water.
Zhang <i>et al.</i> ^[27]	2006	PSI	25 and 100	Effects of diffusion media type and flow field design on the relationship between material properties, liquid accumulation, and electrochemical performance.
Chen <i>et al.</i> ^[28]	2007	NIST	100	Water distributions in anode and cathode GDLs. Flow fields shifted by a channel width allowed separation of water content on either side of fuel cell.
Fu <i>et al.</i> ^[29]	2007	NIST	25	Correlation of cell temperature and water content during start-up.
Hussey <i>et al.</i> ^[30]	2007	NIST	10	Imaging of water distribution normal to the plane of the active area, using a microchannel plate (MCP) detection method with spatial resolution $\approx 30 \mu\text{m}$.
Manke <i>et al.</i> ^[31]	2007	HMI	100	Tomographic imaging of the three-dimensional water distributions in three- and five-cell stacks.
Mukundan <i>et al.</i> ^[32]	2007	NIST	2.25	Imaging normal to the MEA to observe water gradient from inlet to outlet, and relative water content on anode and cathode.
Mukundan <i>et al.</i> ^[33]	2007	NIST	50	Imaging of ice formation during constant voltage operation at -10°C .
Owejan <i>et al.</i> ^[34]	2007	NIST	50	Bypass loop on cathode used to simulate relationship between voltage instability and water content in a multicell assembly.
Owejan <i>et al.</i> ^[35]	2007	NIST	50	Effects of GDL properties, and channel geometry and surface contact angle on water accumulation.
Hartnig <i>et al.</i> ^[36]	2008	HMI	100	Combined neutron imaging with current distribution enabled correlation between local performance and hydration condition.
Hickner <i>et al.</i> ^[37]	2008a	NIST	50	Correlation of water distribution to local cathode flow and temperature conditions.
Hickner <i>et al.</i> ^[38]	2008b	NIST	16.2	High-resolution imaging of water gradients normal to MEA.
Turhan <i>et al.</i> ^[39]	2008	PSU	50	Effects of channel dimensions and land-to-channel width ratio on quantity of retained water.
Ueda <i>et al.</i> ^[40]	2008	JAERI/KURRI	25	Correlation of channel-level water in anode and cathode to cell voltage performance.
Owejan <i>et al.</i> ^[41]	2008	NIST	50	Water distributions under relatively cold operating conditions, and dynamics of cathode air purge.

- HMI: Hahn-Meitner Institute, Berlin, Germany
- JAERI: Japan Atomic Energy Research Institute, Ibaraki, Japan
- KAERI: Korea Atomic Energy Research Institute, Dae-Jong, Korea

- KURRI: Kyoto University Research Reactor Institute, Osaka, Japan
- NIST: National Institute of Standards and Technology, Gaithersburg, Maryland, USA
- PSI: Paul Scherer Institute, Villigen PSI, Switzerland

- PSU: Pennsylvania State University, University Park, Pennsylvania, USA.

This article provides an overview of the applications of neutron imaging to fuel cell technology in the following primary areas: water gradients normal to the MEA; water management in the GDL and flow fields; multicell and transient phenomena; and low temperature and freeze (Section 3). In Section 4, we also discuss some of the future trends in neutron imaging methods, including tomography, high-resolution detectors, and phase imaging.

2 EXPERIMENTAL SYSTEM CONFIGURATION

2.1 Neutron imaging technique and apparatus

There are two primary neutron production mechanisms for use in neutron scattering research: fission and spallation. In both cases, the neutron initially has a kinetic energy of order megaelectron volt (MeV). This energy must be reduced to order millielectron volt (meV) to have appreciable interaction with matter. There are two energy ranges generally used for neutron radiography of fuel cells. The first is the thermal energy range, which has a mean value of 25 meV. The second is the cold neutron energy range, which corresponds to energies of 5 meV and lower. This reduction

in energy is achieved by down scattering in a moderator material, such as water, heavy water, or liquid hydrogen. A neutron beam is formed by allowing the moderated neutrons to escape through a tube that penetrates the radiation shielding into the moderator. To form a neutron imaging beam, an aperture is placed between the neutron source and the sample position, as shown in Figure 1.

A neutron radiograph is a spatially resolved neutron transmission measurement of an object. Neutrons scatter from or are absorbed by the nucleus of an atom, which presents an appreciable total cross-sectional area (σ) for neutron interaction. For thermal neutrons of 25 meV, the total bound cross sections for hydrogen, deuterium, and aluminum are 82.0×10^{-24} , 7.64×10^{-24} , and $1.5 \times 10^{-24} \text{ cm}^2$, respectively.^[42] For water at 300 K, the measured total scattering cross section at the same incident neutron energy is $37.65 \times 10^{-24} \text{ cm}^2$. The total transmission (T) of neutrons through an object composed of isotopes i is determined from the number density N_i , the thickness of material t_i , and σ_i , and is given by the Lambert–Beer law:

$$T = \frac{I}{I_0} = e^{-\sum_i (N\sigma t)_i} \quad (1)$$

The spatial resolution of a neutron image is defined as the minimum spatial separation required to resolve two pointlike objects that have been blurred by the imaging

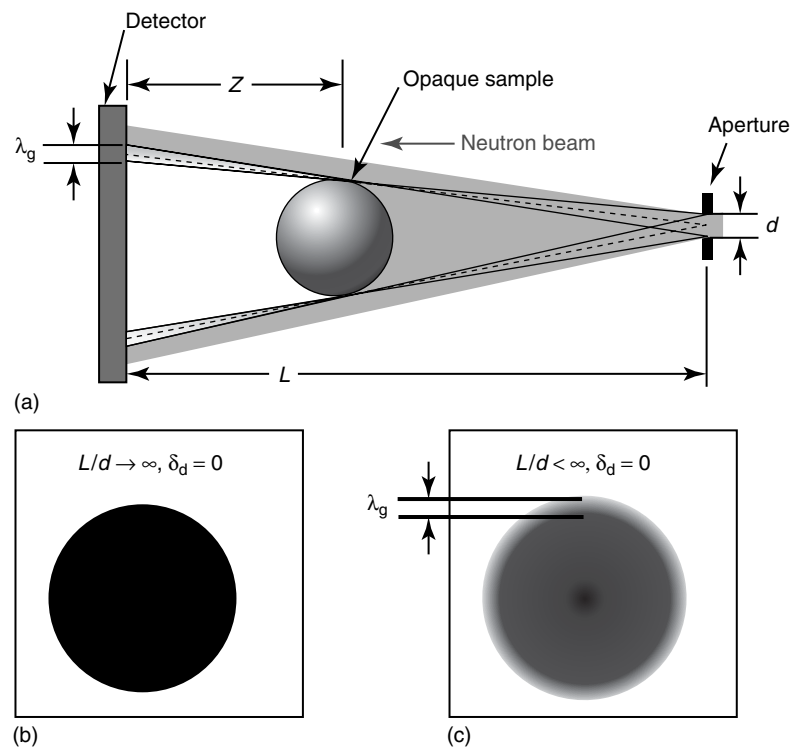


Figure 1. Details of neutron imaging configuration: (a) schematic of the essential components of a neutron imaging facility; (b) an unblurred radiograph of an opaque object; and (c) blurring due to a finite-sized aperture is depicted.

system. The imaging system blur has two primary contributions: the intrinsic detector resolution δ_d and the geometric blur λ_g , due to the neutron beam configuration. λ_g is defined as the image of the aperture if it were imaged by a pinhole at the object separated from the detector by a distance z :

$$\lambda_g = \frac{zd}{(L-z)} \approx \frac{zd}{L} \quad (2)$$

The spatial resolution of the image due to the geometry of neutron beam setup (see Figure 1) is determined by the aperture diameter d and the detector–aperture separation distance L . For a typical PEMFC imaging system, $L/d \geq 300$ is necessary for resolving water in the channels relative to the lands and a value of 600 is nearly optimal when using a standard neutron radiography camera (the spatial resolution for a standard camera is about $250 \mu\text{m}$). Improving or increasing L/d by either decreasing d or increasing L reduces the neutron intensity, which corresponds to longer image acquisition times. For high-resolution neutron radiography detectors, much higher values of L/d ($L/d \geq 1200$) are necessary. The image blur resulting from δ_d is due to the details of the neutron detection. The primary detector for neutron imaging is a ZnS scintillator loaded with a neutron absorber such as ^6Li coupled to a light detector. The neutron capture event results in a charged particle that deposits energy into the ZnS, which emits scintillation light in all directions. This uniform light emission limits δ_d to about the thickness of the scintillator, which is typically $100\text{--}300 \mu\text{m}$. The scintillation light is captured by a digital imaging device such as a charge-coupled device (CCD) or an amorphous silicon panel. The overall image resolution is $(\lambda_g^2 + \delta_d^2)^{1/2}$, and, for typical values of $z = 10 \text{ cm}$, $L/d = 600$, and $\delta_d = 250 \mu\text{m}$, gives an overall spatial resolution of about $300 \mu\text{m}$.

The spatial resolution determines how well one can distinguish PEMFC components in the image plane, but the measurement uncertainty of the liquid water thickness is equally important. The liquid water thickness is obtained by processing images using equation (1), combined with knowledge of the liquid water neutron attenuation $N_w\sigma_w$. Because σ_w depends on neutron energy, a calibration measurement of $N_w\sigma_w$ for each configuration is required. A dry and wet image of a water wedge with varying thicknesses is taken, and a linear relationship to directly apply equation (1) or to form a look-up table is assumed.^[9] Because the water thickness is determined by the ratio of a wet and dry image, it is important to account for potential fluctuations in the incident neutron fluence during the two image acquisitions. The standard method to accomplish this is to normalize the wet image to the dry image using the average pixel intensity in an unobstructed or unchanging portion of the image. The sequence of image-processing

steps required to extract quantitative water thickness data from a neutron radiograph is illustrated in Figure 2.

The uncertainty in the water thickness, δt_w , is composed of random and systematic contributions. The random uncertainty is the fundamental limit to the measurement accuracy and is determined by Poisson neutron counting statistics (also known as *shot noise*):

$$\delta t_w \approx \frac{1}{N_w\sigma_w} \sqrt{\frac{2}{I_0AT\eta}} \quad (3)$$

where I_0 is the incident fluence rate ($\text{cm}^{-2} \text{s}^{-1}$), A is the integration area, T is the integration time, and η is the neutron detection efficiency.^[43] The systematic uncertainties come primarily from neutron scattering, unstable fuel cell performance during the integration time, and unintended motion of the fuel cell between dry and wet images. Image blur can also contribute to a systematic error in the thickness and has been discussed at length by Kramer *et al.*^[8] With long integration times, the systematic uncertainties can dominate the total water thickness uncertainty, but are to some extent under the control of the experimenter, as described in Section 2.2.

2.2 Fuel cell test article considerations

In contrast to other liquid water diagnostics, neutron radiography requires minimal changes to the PEMFC hardware. Most designs are directly compatible as graphite, aluminum, stainless steel, and thin electrical insulation have at least an order of magnitude smaller σ than water, allowing sufficient neutron transmission to detect thin liquid water layers. However, optimizing the test hardware for neutron imaging results in increased spatial and temporal resolutions, as well as decreased systematic uncertainties associated with calculating the liquid water content.

The most common experiments probe liquid water in-plane across the active area. For such experiments, there are three important design considerations: use materials with small σ , reduce the thickness of materials with larger σ , and use a flow field design that allows for anode and cathode channel discrimination.^[4, 28, 35] Graphite flow distributors used in some experiments^[11, 17] revealed the necessity of sealing the porous material from liquid water permeation. Gold-plated aluminum flow fields improve image quality; however, cell durability can be impacted as this material combination corrodes when exposed to deionized water at fuel cell potentials. More durable flow distributors can be manufactured from thin stainless steel or sealed graphite. Because any test article movement, including that due to thermal expansion, causes the reference to be misaligned, thus introducing image artifacts, mounting the cell in the beam should be integral to the overall design. Specifically,

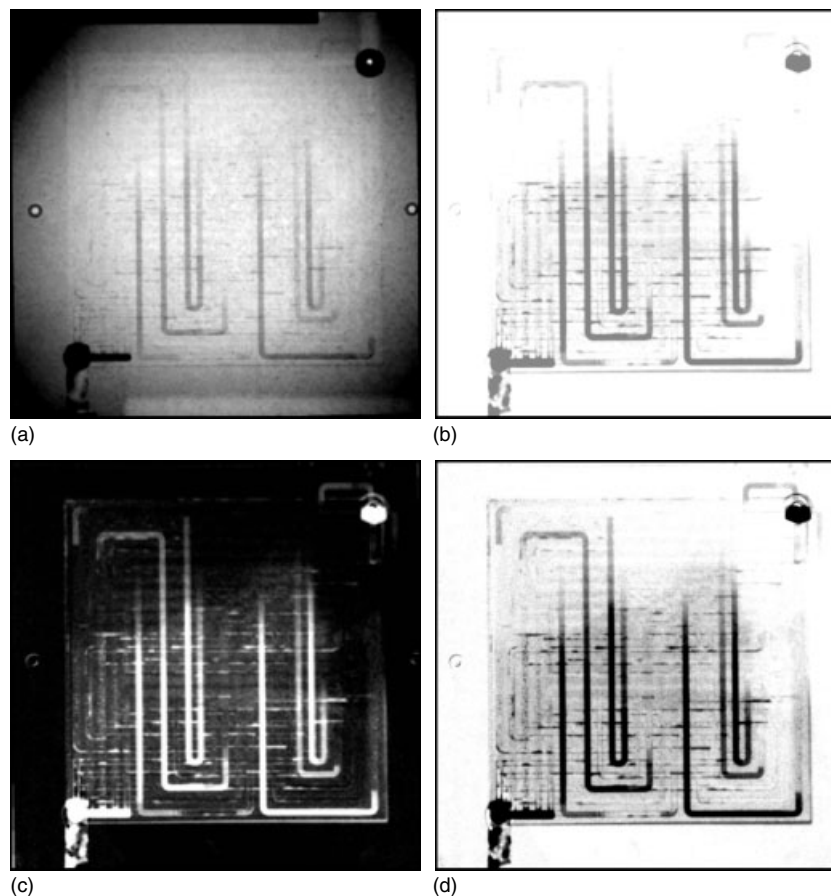


Figure 2. Sequence of steps in neutron radiograph image processing: (a) raw radiograph of operating fuel cell; (b) normalization by dry image; (c) negative natural logarithm of pixel intensity, as per equation (1); and (d) image averaging and mapping to black monochrome color scale.

the fixture should be rigid, isolated from vibration, and resistant to conductive heat transfer from the cell for accurate dry system normalization.

Temperature regulation of the fuel cell for neutron radiography should also be optimized. Heating elements should be removed from the line of sight through the active area because of their wide fluctuations in temperature that cause localized movement and variation in the scattered neutron intensity. When using liquid cooling in the active area plane, a favorable alternative to water or glycol is heavy water (deuterium oxide, D_2O). The thermal and chemical properties of D_2O are nearly identical to that of water, but D_2O has a much smaller σ than water. To control the temperature of the test section below $0^\circ C$, a mixture of water (or heavy water) and ethylene glycol is required. Deuterated ethylene glycol is commercially available; however, the high cost makes this a less attractive option. Also, to prevent frost formation on the outside of the test section and thus image artifacts, freeze testing should be performed inside a humidity-controlled environment.

High-resolution through-plane imaging and tomographic imaging have similar mechanical design challenges.

Assumptions used to quantify liquid water content from the measured neutron attenuation using equation (1) no longer apply when the integrated water thickness exceeds about 1 mm.^[43] This places a design restriction on the width of the active area so that the maximum possible saturation contains less than 1 mm of water. Minimizing the width improves the resolution by allowing the imaging plane to be closer to the detection plane; i.e., reducing z in equation (2). Gasket material selection is also an important consideration when the active area plane is parallel to the neutron beam. Expanded polytetrafluoroethylene (PTFE) and aluminum are possible low-attenuating alternatives to rubber- and silicone-based materials.

3 APPLICATIONS OF NEUTRON IMAGING

3.1 Water gradients normal to the membrane-electrode assembly (MEA)

Measuring the through-plane water distribution (i.e., from anode gas channels through the membrane to the cathode

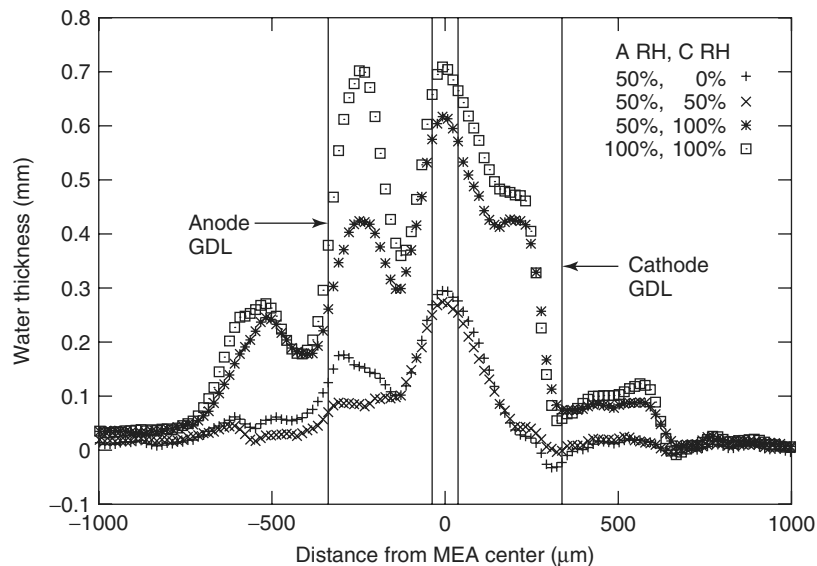


Figure 3. A comparison of the through-plane water distributions at different anode and cathode inlet relative humidity. Operating conditions: current density = 1.0 A cm^{-2} , $T = 80^\circ \text{C}$, $P = 100 \text{ kPa}$, and anode/cathode stoichiometric ratios of 1.1/2.^[32]

channels) is important for understanding the fundamentals of mass transport and its effects on the electrochemical performance of PEMFCs. While the first demonstration of neutron imaging to study fuel cells was for measuring the water gradient across the membrane,^[2] there has since been little work on this topic. The few articles that have been published are predominantly focused on observation and have not yet been directly connected to any modeling effort. The main reason for the relatively few efforts is that the image resolution historically achievable with scintillators is about $250 \mu\text{m}$, which is insufficient to resolve the MEA water profile or that in standard gas diffusion layers (GDLs).

The first reported fuel cell neutron imaging measurement was of the water content in an artificially thick membrane formed by thermally bonding four Nafion 117^{®a} membranes (each $150\text{-}\mu\text{m}$ -thick perfluorosulfonic acid).^[2] The trend of the water gradient was to increase from the anode to cathode, but it was not a monotonic increase as expected, as local maxima and minima were observed and attributed to the less hydrophilic surface of each individual Nafion[®] membrane. The difference in neutron intensity between the maxima and minima was several times that of the root mean square deviation of the intensity, and so was statistically significant.

There was one attempt to measure the through-plane water distribution using tomography.^[13] In this study, the test section had an active area of $1 \text{ cm} \times 4 \text{ cm}$ and used 1-mm -thick GDLs and a Nafion 117[®] membrane. A scintillator detector system was used, and the reconstructed image resolution was about $250 \mu\text{m}$. Despite this coarse spatial resolution, these experiments clearly demonstrated water gradients within the GDLs.

Recently, there have been two published results of the through-plane water distribution measured with a spatial resolution of $25 \mu\text{m}$. The first experiment was a demonstration of new imaging technology based on a microchannel plate (MCP) detector, discussed further in Section 4.^[30] The test section had a narrow active area, $0.4 \text{ cm} \times 25 \text{ cm}$, so as to minimize λ_g (equation 2), with a Nafion 117[®] membrane and 1-mm -thick GDL. The cell had relatively high anode and cathode flow rates so as to prevent water accumulation in the channels. The other study of through-plane water content was focused on the effect of the PTFE content in the bulk substrate and microporous layer (MPL) of three different carbon fiber GDLs on the cathode.^[32] The fuel cell had an active area of 2.25 cm^2 , and the depth of the flow channel was chosen to yield a pressure drop near to that of a standard 50-cm^2 cell. Neutron radiography of the through-plane water content revealed that higher PTFE content in the cathode MPL resulted in more flooding, and thus a significant reduction in oxygen mass transport to the cathode. Also, as shown in Figure 3, the inlet relative humidity has a large influence on the water content within the anode and cathode GDLs. The total water content is at a maximum level with both inlet streams fully humidified. Reducing the anode inlet relative humidity (RH) to 50% reduced the maximum amount of trapped water between the anode GDL and channel to about 40% of the fully saturated state, whereas the membrane water content was only reduced to 86% of the saturated state. A more dramatic reduction (14% of the fully saturated case) was observed by reducing the cathode inlet RH to 50%. The average membrane water content in this case was also dramatically reduced by about 60%, demonstrating that the cathode inlet RH plays a major role in the water retention of the cell.^[32]

3.2 Gas diffusion layer (GDL) water management

Neutron radiography has been used to investigate several factors that influence the water retention in the GDL, grouped in three main categories: GDL structure (permeability, pore size distribution, MPL, and PTFE loading); gas stream conditions (inlet RH, flow rate, and pressure); and cell construction and operating conditions (channel geometry, channel surface energy, bulk temperature, heater placement, and current density history). One general finding is that there is no single, monotonic relationship between the GDL water retention and the current density. Rather, there is a complex interplay between all three primary factors.

The porous media properties of the GDL are fundamental to the water transport from the catalyst layer to the channel. The use of an MPL is known to improve the performance of a PEMFC (see **Diffusion media materials and characterisation**, Volume 3). However, by increasing the PTFE content of the MPL, one reduces the open pore volume, which can increase mass transport resistance on the cathode. Also, the increased hydrophobicity of the additional PTFE may also drive water back into the MEA. Other studies examined different PTFE loadings in the MPL and bulk of the GDL, and from polarization curves determined that there is an optimum PTFE loading in the MPL for a given GDL substrate.^[26, 32] Neutron radiography was applied to demonstrate that the loss in performance was attributable to an increase in the GDL water retention.

The pore size distribution also seems to play a role in the GDL water retention, at least when comparing paper GDL to cloth GDL, each with an MPL.^[16, 26] In both studies, the overall cell water retention was about equal, but the paper GDL showed a lower limiting current. Using mercury porosimetry, the paper pore distribution showed a narrow peak corresponding to a bulk pore size of about 50 μm , while the cloth GDL showed a broad pore size distribution from a few micrometers up to about 100 μm . In the cloth GDL, the water preferentially filled the larger pores (smaller surface-to-volume ratio), leaving the smaller pores open for oxygen transport to the catalyst layer. The open pore volume plays an important role in the cell performance. It seems that there is a critical GDL saturation at which point the GDL begins to reject water into the channels, and resistance to oxygen transport to the MEA reaches its maximum.^[19, 20, 34, 35] In extreme cases, this can lead to cell failure (see, e.g., **Electrode degradation mechanisms studies by current distribution measurements**, Volume 6) or, in voltage controlled experiments, a significant reduction in the current density.

The inlet gas stream can remove water either through evaporation or convection, and can introduce water to the fuel cell in the vapor phase. A widely observed trend for experiments that run in a coflow orientation is that the

region near the gas inlet is drier than that near the outlet, as the gas stream becomes saturated from the removal of product water down the channel. One study demonstrated that, at high current density, significant mass transport loss can result from very small changes in liquid water content, indicating that interfacial water (likely forming between the GDL and electrode layers) is a key contributor.^[6]

The thermal environment of the GDL impacts the overall liquid water retention, particularly the waste heat from the electrochemical reaction which enhances evaporative water transport from the MEA to the channels. In addition to the waste heat, the placement of cartridge heaters can alter the water content in the flow fields, suggesting that the usual assumption of uniform temperature distribution across the flow field is not always valid.^[26] The impact on water retention is that this “local heating” can be a source of additional drying of the fuel cell.^[11] Thus, it is possible that as the current density is increased, the waste heat aids in the evaporation at the MEA, resulting in a drier cell.

Another general trend observed through neutron radiography is that the change in water content of the GDL occurs slowly, especially compared to changes in the rate of water production.^[11, 16, 19] An aspect of this slow response is that one can observe a hysteresis in the water content during sweep up and down of the current density.^[25, 26] For a given reactant stoichiometry, the critical saturation may only occur near the limiting current. As the current is reduced from near limiting current, there may not be sufficient gas flow to remove the liquid from within the GDL. This extra water yields a smaller open pore volume and reduced oxygen transport to the catalyst layer.

3.3 Flow field water management

The characteristic length scale of bipolar plate channels typically ranges from 0.5 to 1 mm (see **Serpentine flow field design**, Volume 3), so the neutron imaging method is well suited to study steady-state and transient phenomena in this part of the fuel cell. It is difficult to ascertain in a two-dimensional radiograph the anode versus cathode location of channel-level water, unless the flow fields are specifically designed to permit this determination. For example, flow fields can be arranged perpendicularly, so that anode and cathode channels are offset by 90° over most of the active area.^[4, 35] Also, separate anode and cathode water quantification can be enabled by shifting the flow fields by one channel width.^[28]

Much of the research involving neutron imaging of fuel cells has been applied to studying water accumulation in different channel geometries. Many articles have reported the persistent problem of trapping water in the U-bends of serpentine flow fields,^[9, 21] which occurs as a result of gas bypass across the lands, through the porous GDL.

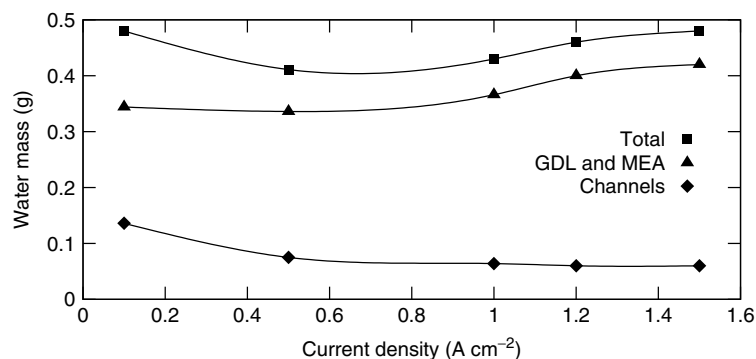


Figure 4. Water mass as a function of current density, for a 50-cm² cell built with MEA from W.L. Gore & Associates (25 μm Nafion[®], Pt areal density of 0.4 mg cm⁻² on anode and cathode) and SGL 21BC gas diffusion layers. Operating conditions: $T = 80^\circ\text{C}$, $P = 200\text{ kPa}$, fully humidified reactant with anode/cathode stoichiometric ratios of 2/2.^[4]

Yoshizawa *et al.*^[26] studied how disruption of gas flow can be correlated to lower performance with different flow channel geometries. Water accumulation has also been shown to affect interdigitated flow fields. Although such designs afford the possibility of reducing mass transport losses by forcing convective reactant flow through the GDL, liquid water tends to accumulate at the closed ends of the channels,^[8, 19] and can only be effectively eliminated through evaporation.

A common observation in literature describing the water content and distribution in an operating fuel cell is the correlation between current density and total measured water volume.^[9, 23, 25] Low current densities present the greatest risk of channel-level flooding due to the lower reactant gas flow rates, which do not have as much potential to remove liquid water droplets and slugs from the cell. Channel flooding at low current density is further exacerbated by using saturated gas flows and low reactant stoichiometries. Several studies have shown that independent of cell size, materials, and flow field geometry, increasing gas shear is an effective means of removing liquid water from channels,^[15, 17, 23] (see **Serpentine flow field design**, Volume 3).

A method commonly used to distinguish between water accumulating over or in the channels and the water accumulating over the lands is to develop image masks that remove the contribution to the overall water volume from a portion of the geometry. Such masking methods enable separate analysis of water holdup in channels and nonchannel regions of the fuel cell. An example is illustrated in Figure 4, where the water content in a 50-cm² fuel cell was analyzed to determine the fraction of water contained within the flow field versus that residing in the porous GDL and MEA materials. From such analysis, it is possible to study channel water management over the entire range of operating conditions and determine under what conditions water can introduce performance anomalies, as discussed in Section 3.4.

Channel cross-sectional geometry and surface energy are important design considerations, as these properties influence the overall amount of liquid water retained, and the degree to which individual channels become blocked. Turhan *et al.*^[23] conducted experiments in which different quadrants of the anode and cathode flow fields were either hydrophilic from the gold-plated aluminum surface, or rendered hydrophobic from a secondary coating applied to the channel walls only. Owejan *et al.*^[35] investigated the combined effects of channel geometry (rectangular and triangular with the same cross-sectional area) and surface energy. Neutron imaging showed that the quantity of retained channel water, and the morphology of the water droplets, is most strongly affected by the channel geometry rather than surface energy. As shown in Figure 5, for horizontally oriented cathode channels, the rectangular geometry retains relatively large slugs, which fill a large fraction of the channel cross section. In contrast, the triangular flow field tends to retain smaller droplets in pairs, which are captured in the 43° angles formed between the flow channels and diffusion media.

3.4 Multicell and transient phenomena

Neutron radiography studies are not limited to material and channel evaluations, but can also be applied to study multiple cells that experience temperature transients during start-up, shutdown, and load changes. Although these transients may represent only a small portion of the overall operating time, the resulting residual liquid water impacts performance and durability. Early work by Geiger *et al.*^[3] investigated the effect of start-up and shutdown temperature transients on water accumulation in a 100-cm² test cell. The start-up from 20 °C with dry inlet gas streams in a coflow orientation was shown to quickly accumulate liquid water near the gas outlets. As the experiment progressed and the cell temperature increased, the liquid water

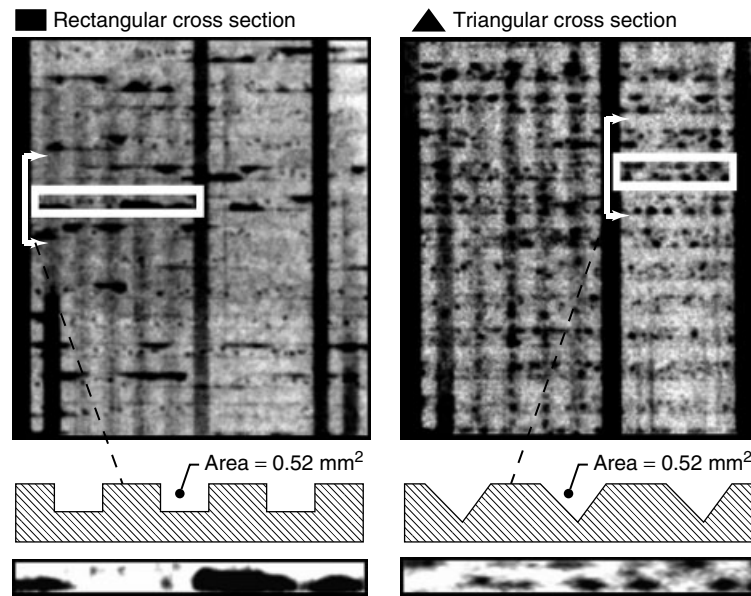


Figure 5. Influence of channel cross-sectional geometry on morphology of water droplets in horizontal cathode channels at low current density. Rectangular channels tend to form larger slugs, which fill much of the channel cross section, while triangular channels tends to form droplets in pairs, residing in the corners between the flow field and the gas diffusion layer. The 50-cm² fuel cell was operated with the anode flow field arranged orthogonally to the cathode, and built with a 25- μ m membrane, anode and cathode Pt areal density of 0.4 mg cm⁻², and Toray 060 gas diffusion layers. Operating conditions: $T = 80^\circ\text{C}$, $P = 200\text{ kPa}$, fully humidified reactant with anode/cathode stoichiometric ratios of 2/2. [Reproduced from Ref.[35]. © Elsevier, 2007.]

content peaked, after which further temperature increases resulted in reduced liquid water content as the gas streams were capable of carrying more product water in the vapor phase.

Water accumulation during a start-up transient was also investigated by Fu *et al.*,^[29] but with humidified gases instead of dry, more closely representing a fuel cell system with external humidification. Because saturation concentration increases significantly with temperature, difference in water content for dry and saturated inlet gas streams at room temperature is small relative to the reaction product water flux. At higher temperatures, the water content in saturated gas becomes significant and the evaporative capacity of dry gas is much higher, hence the need for external humidification. With saturated inlet gas, the difference in evaporation rate is minimized during the temperature transient. However, it was shown by both Fu *et al.* and Geiger *et al.* that the fuel cell power output initially increases due to faster reaction kinetics at higher temperature. As liquid water volume increases, mass transport losses begin to impact power output. A sketch of the general behavior is shown in Figure 6.

Liquid water accumulation in a fuel cell system is further complicated by small differences in flow resistance among multiple cells. If one cell in a group of hundreds becomes blocked with liquid water or ice, a gas flow maldistribution may result. For this reason, neutron imaging experiments have been conducted to more accurately represent multicell behavior. Liquid water in a small-scale four-cell

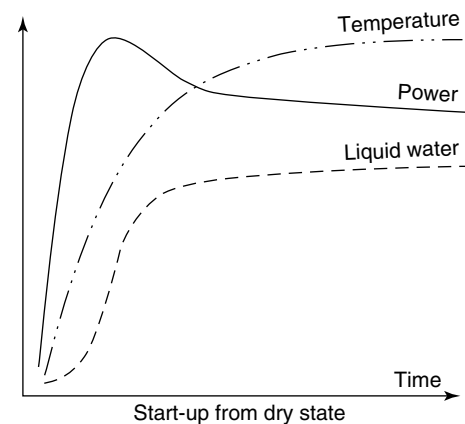


Figure 6. Room temperature start-up behavior in relation to liquid water accumulation.

PEMFC assembly was first considered by Satija *et al.*,^[5] where two-dimensional radiography and three-dimensional tomography methods were applied. These experiments identified the nonuniform liquid water accumulation that occurs in a multiple fuel cell assembly by quantifying total GDL and channel water content. Three-dimensional tomographic imaging of a PEMFC was further investigated by Manke *et al.*^[31] with three-cell and five-cell assemblies. The results indicate significant variations in the liquid water content among the individual cells, with the end cells generally having more retained water due to heat loss. Higher liquid water content was further correlated to cell voltage as these

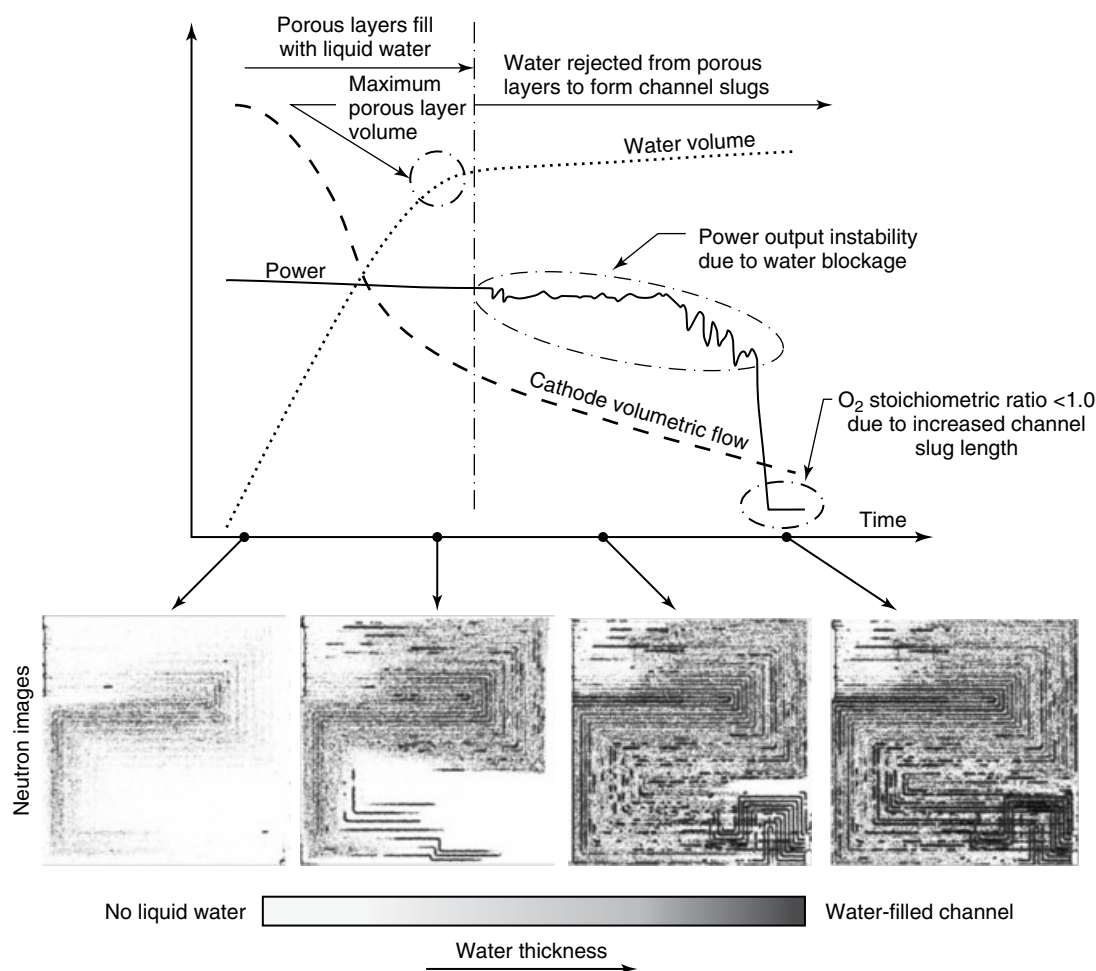


Figure 7. Simulated multiple fuel cell response to water accumulation transient. As liquid water accumulated, the associated increase in flow resistance resulted in a drop in the oxygen stoichiometric ratio.

cells were shown to operate at lower power due to increased mass transport limitations.

Although tomography can provide three-dimensional water content, these experiments lack the temporal resolution required to capture transient behavior, as a typical tomography scan takes 10 min or more. To overcome this limitation, Owejan *et al.*^[34] simulated the dynamics of a 20-cell assembly using a single fuel cell and a bypass loop. In the dry state, the flow resistance of the bypass loop was adjusted such that 1/20 of the gas flow was supplied to the cell at a given stoichiometric ratio. The cell was then operated at low current density to investigate idle conditions where liquid water is most likely to stagnate in the flow field channels due to low gas shear, as shown in Figure 7. Water accumulated in two distinct modes, as evidenced by a change in the water-retention rate. From the initial dry state, liquid water first accumulated in the GDL at a rate slightly less than the water production rate, continuing to fill until a critical saturation fraction was reached. At this point, liquid water was

rejected into the gas flow channels and began to form stagnant liquid slugs. As these slugs increased in length, the oxygen stoichiometric ratio decreased due to higher flow resistance. Eventually, the stoichiometric ratio became insufficient to support the electrochemical reaction and the power output of the cell dropped. The fundamental mechanism that eventually caused this power loss is present in all multicell assemblies that are operated with saturated outlets, but the effect cannot be adequately represented with a standard single-cell experiment.

Correlating the neutron radiography data to voltage feedback of a cell operated at constant current can give useful insight on how liquid water affects the stability. Ueda *et al.*^[25] found that cathode water slugs caused voltage instability while the slugs remained in the flow fields. Once the slugs were removed from the active area, the voltage recovered above the previous voltage level for a period of time before returning to the average steady-state value. Dynamic water slugs did not affect the voltage when observed on the anode side of the cell.

3.5 Low temperature and freeze performance

For automotive applications in particular, it is necessary to understand water transport behavior under low temperature and freezing conditions. Even though many systems are optimized to operate near 80 °C, for short drives at low ambient temperature, the fuel cell may not heat up to its optimal steady-state condition. Moreover, for conditions where ice formation occurs, the fuel cell start-up needs to be controlled such that the waste heat can effectively bring the cell temperature above 0 °C before product water fills and freezes in pores in the electrodes, thereby blocking reactant gas flow to the catalyst (see **Cold-start durability of membrane-electrode assemblies; Performance during start-up of proton exchange membrane (PEM) fuel cells at subfreezing conditions**, Volume 6). To apply neutron radiography for low temperature and freeze testing, an enclosed environmental chamber is required to prevent condensation and frost from forming on the fuel cell. Such a system has been installed at NIST, with an operating temperature as low as -40 °C and a cooling power of 1 kW at this temperature. The sample chamber “windows” are thin aluminum sheets, which introduce an additional 6.5 mm of aluminum to the neutron flight path. The water attenuation changes with temperature. This results primarily from the change in number density (N_w) rather than a change in neutron cross section (σ_w), which would be expected if there was a change in molecular motion. While N_w changes with temperature, it is not possible to know the physical state of H₂O from a single neutron radiograph. Rather, the presence of liquid can only be inferred, for instance, if there is noticeable motion of a liquid water channel slug.

To investigate the water transport fundamentals of fuel cells under relatively cold conditions, a 50-cm² test apparatus was designed to represent the aspect ratio and flow field geometry of practical fuel cell hardware, in accordance with performance targets published by the US Department of Energy.^[44, 45] In Figure 8, neutron radiographs are shown for this apparatus operated at temperatures of 35, 45, and 55 °C with fixed voltages of 0.9, 0.8, and 0.7 V, respectively. Water distributions are shown for the electrochemical active area only, in counterflow operation with the cathode inlet on the left and anode inlet on the right of each figure. It was observed that the water content decreased monotonically with increasing temperature, but that the most significant water holdup, at both the channel-level and within the GDL/MEA layers, occurred at moderate voltage (0.7 V). At low temperatures, the water-carrying capacity of the reactant streams is reduced, and therefore less product water can be removed in the vapor phase.^[45] As discussed in Sections 3.2 and 3.3, the water present in the fuel cell is a complex function of the operating conditions, materials, and the cell voltage, the latter dictating the amount of waste heat produced. These results clearly indicate that mapping the water volume over the low-temperature portion of the overall fuel cell operating envelope is needed to fully characterize performance and phenomena that can contribute to material degradation.

The first *in situ* neutron radiography of a freeze-start was of the in-plane water (or ice) distribution of a single serpentine, 50-cm² cell operated at -10 °C reported by Mukundan *et al.*^[32] The retained water compared to the product water based on the cumulative current indicated that all the product water was frozen inside the cell. Since the

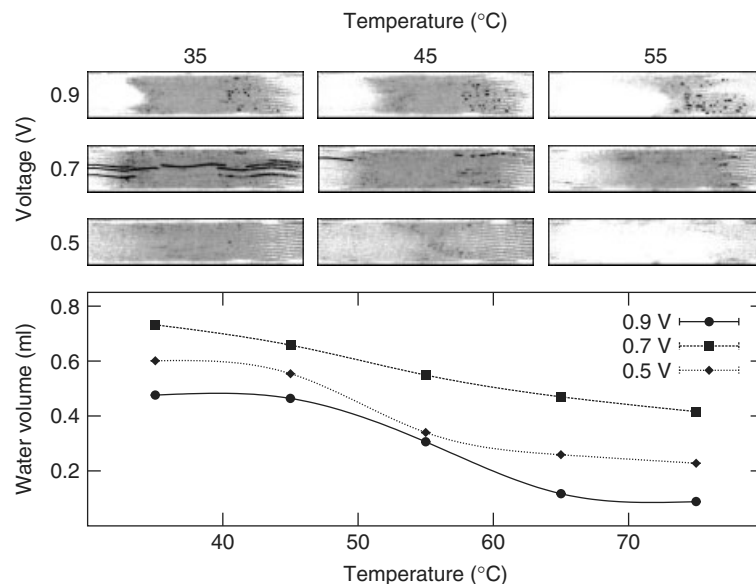


Figure 8. Effect of cell operating temperature on water accumulation. At each voltage, the experiments were conducted with the same stoichiometric ratios and inlet relative humidity of 50%.

measurement was in-plane, it was not possible to determine in which component the ice was forming.

4 NEUTRON IMAGING: FUTURE DIRECTIONS

Near-term advances in PEMFC neutron imaging will be dominated by recent improvements in neutron detector spatial resolution. High-resolution neutron radiography will enable direct, *in situ*, measurement of the through-plane water distribution at steady state. Traditional scintillator technology has a spatial resolution of between 100 and 250 μm . This is due to the requirement of high neutron capture efficiency (about 20%) that increases with increasing thickness balanced against sufficient light output and spatial resolution, both of which decrease with increasing scintillator thickness. There is current research into new scintillator binder materials that enable comparable neutron capture efficiency and high light output with thinner scintillators, and may result in spatial resolutions approaching 25 μm .^[46] MCP detectors have been shown to have a spatial resolution of 25 μm ,^[47] which was limited by the channel diameter. The next generation of MCPs for neutron detector applications will have about a 5- μm channel diameter, and anticipated spatial resolution of 10 μm .^[48] A further improvement in the spatial resolution might be obtained by utilizing a detection method based on neutron depth profiling.^[49]

One of the challenges of high-resolution neutron radiography is that the neutron intensity in a pixel decreases as the square of the change in the spatial resolution. Therefore, to achieve the same measurement uncertainty in a 10- μm pixel as in a 100- μm pixel, a 100 \times longer image exposure time is required. Future neutron imaging facilities in the locations summarized in Section 1 may realize some advantages to using lower energy neutrons (known as *cold neutrons*^[50]) for PEMFC imaging. To date, most PEMFC imaging has been conducted at thermal neutron imaging facilities. Cold neutrons have higher transmission through some metals because the energy is too low to be scattered by the metal crystal lattice (Bragg scattering). In contrast, the neutron attenuation due to water increases with decreasing neutron energy, yielding increased sensitivity to water. Furthermore, the detection efficiency of cold neutrons is about a factor of 2 larger than that of thermal neutrons, which would help reduce the image acquisition time for high spatial resolution detectors.

Cold neutrons also provide the opportunity for a different imaging technique known as *neutron phase imaging* or *phase radiography*.^[51] The source of contrast with phase radiography is very different from transmission radiography, and, in some cases, can provide a much higher contrast than transmission radiography. Although to date there are

no published examples of neutron phase imaging of PEMFCs, there may be future applications using high-resolution imaging, such as measurement of the membrane hydration using heavy water (D_2O), material interfaces, and normal stresses in stamped flow field plates. One reason for phase radiography not being used as a technique for PEMFC research is due to low source intensities. There is current research into developing methods with high-intensity cold neutron sources.^[52]

Radiography is a two-dimensional (2-D) measurement. To measure the water distribution in three dimensions, such as in multiple cells, one must use tomography. Tomography requires that the object under study be rotated through 180°, with radiographs taken at a number of projection angles, which scale linearly with the size of the object. These 2-D radiographs are traditionally processed with the filtered back-projection algorithm to produce a three-dimensional map of $N\sigma$.^[53] In addition, to avoid reconstruction artifacts, tomography requires that the test section be operated at steady state, or that the gas flows be ceased to maintain the water distribution, which imposes the assumption that capillary forces are sufficiently weak to not change the water profile in the GDL. The acquisition time to obtain the required number of projections for two published studies was 20 min for a small PEMFC with active area 1 cm \times 4 cm at the NIST facility,^[13] and about 5 h for a 10 cm \times 10 cm PEMFC at the HMI facility.^[31] By using statistical tomographic reconstruction techniques such as maximum-likelihood,^[54] it might be possible to reduce the tomographic image acquisition time by acquiring fewer projections.

ACKNOWLEDGMENTS

The authors would like to acknowledge the contributions of Mr Eli Baltic in developing and maintaining the experimental facility at NIST, and Dr Patrick Gallagher (NIST) and Dr Mark Mathias (GM) for their active support of the fuel cell neutron imaging program. This work was supported by the US Department of Commerce, the NIST Ionizing Radiation Division, the Director's office of NIST, the NIST Center for Neutron Research, and the Department of Energy through interagency agreement no. DE-AI01-01EE50660.

END NOTES

^a. Certain trade names and company products are mentioned in the text or identified in an illustration in order to adequately specify the experimental procedure and equipment used. In no case does such identification imply recommendation or endorsement by NIST, nor does it imply that the products are necessarily the best available for this purpose.

REFERENCES

1. J. St-Pierre, *J. Electrochem. Soc.*, **154**, B724 (2007).
2. R. J. Bellows, M. Y. Lin, M. Arif, A. K. Thompson and D. Jacobson, *J. Electrochem. Soc.*, **146**, 1099 (1999).
3. A. B. Geiger, A. Tsukada, E. Lehmann, P. Vontobel, A. Wokaun and G. G. Scherer, *Fuel Cells*, **2**, 92 (2002).
4. J. P. Owejan, 'Neutron Radiography Study of Water Transport in an Operating Fuel Cell: Effects of Diffusion Media and Cathode Channel Properties'. M.S. Thesis, Rochester Institute of Technology (2003) <http://hdl.handle.net/1850/5279>.
5. R. Satija, D. L. Jacobson, M. Arif and S. A. Werner, *J. Power Sources*, **129**, 238 (2004).
6. P. A. Chuang, A. Turhan, A. K. Heller, J. S. Brenizer, T. A. Trabold and M. M. Mench, 'The Nature of Flooding and Drying in Polymer Electrolyte Fuel Cells', "Presented at 3rd International Conference on Fuel Cell Science, Engineering and Technology", Paper FUELCELL2005-74051, Ypsilanti, MI, May 23–25, 2005.
7. T. Kim, Y. Jung, M. Kim, M. Arif, D. L. Jacobson, D. Hussey, C. Sim, S. Lee and J. Jeon, 'The Visualization of Water Distribution at the PEMFC Using the Neutron Imaging Technique: Feasibility Test', "IEEE Nuclear Science Symposium Conference Record", Puerto Rico, USA, Paper N14-127, p. 639, 2005.
8. D. Kramer, J. Zhang, R. Shimoi, E. Lehmann, A. Wokaun, K. Shinohara and G. G. Scherer, *Electrochim. Acta*, **50**, 2603 (2005).
9. N. Pekula, K. Heller, P. A. Chuang, A. Turhan, M. M. Mench, J. S. Brenizer and K. Ünlü, *Nucl. Instrum. Methods Phys. Res., Sect. A*, **542**, 134 (2005).
10. I. A. Schneider, D. Kramer, A. Wokaun and G. G. Scherer, *Electrochem. Commun.*, **7**, 1393 (2005).
11. M. A. Hickner, N. P. Siegel, K. S. Chen, D. N. McBrayer, D. S. Hussey, D. L. Jacobson and M. Arif, *J. Electrochem. Soc.*, **153**, A902 (2006a).
12. M. A. Hickner, N. P. Siegel, K. S. Chen, D. S. Hussey, D. L. Jacobson and M. Arif, 'Exploring Liquid Water Distribution and Local Heating Effects in an Operating Proton Exchange Membrane Fuel Cell', "Proceedings of the 8th World Conference on Neutron Radiography", Gaithersburg, MD, 2006b "Neutron Radiography", M. Arif and R. G. Downing (Eds), DES Tech Publications, Lancaster, PA, pp. 480–486 (2008).
13. D. S. Hussey, J. P. Owejan, D. L. Jacobson, T. A. Trabold, J. Gagliardo, D. R. Baker, D. A. Caulk and M. Arif, 'Tomographic Imaging of an Operating Proton Exchange Membrane Fuel Cell', "Proceedings of the 8th World Conference on Neutron Radiography", Gaithersburg, MD, 2006 "Neutron Radiography", M. Arif and R. G. Downing (Eds), DES Tech Publications, Lancaster, PA, pp. 470–479 (2008).
14. T. Kim, Y. Jung, M. Kim, C. Sim, S. Lee and J. Jeon, *Nucl. Eng. Technol.*, **38**, 449 (2006a).
15. T.-J. Kim, M.-H. Kim and C.-M. Sim, 'Research for Water Removal at PEMFC by Using Neutron Imaging Technique at NRF, HANARO: Feasibility Study', "Proceedings of the 8th World Conference on Neutron Radiography", Gaithersburg, MD, 2006b "Neutron Radiography", M. Arif and R. G. Downing (Eds), DES Tech Publications, Lancaster, PA, pp. 416–424 (2008).
16. J. J. Kowal, A. Turhan, K. Heller, J. Brenizer and M. M. Mench, *J. Electrochem. Soc.*, **153**, A1971 (2006).
17. D. J. Ludlow, C. M. Calebrese, S. H. Yu, C. S. Dannehy, D. L. Jacobson, D. S. Hussey, M. Arif, M. K. Jensen and G. A. Eisman, *J. Power Sources*, **162**, 271 (2006).
18. I. Manke, Ch. Hartnig, N. Kardjilov, M. Grünerbel, J. Kaczerowski, A. Hilger, W. Lehnert and J. Banhart, 'Neutron Radiography and Tomography on Fuel Cells – Recent Developments at CONRAD', "Proceedings of the 8th World Conference on Neutron Radiography", Gaithersburg, MD, 2006.
19. J. P. Owejan, T. A. Trabold, D. L. Jacobson, D. R. Baker, D. S. Hussey and M. Arif, *Int. J. Heat Mass Transfer*, **49**, 4721 (2006a).
20. J. P. Owejan, T. A. Trabold, J. Gagliardo, D. L. Jacobson, R. N. Carter, D. S. Hussey and M. Arif, 'Voltage Instability in a Simulated Fuel Cell Stack Correlated to Water Accumulation Measured Via Neutron Radiography', "Proceedings of the 8th World Conference on Neutron Radiography", Gaithersburg, MD, 2006b "Neutron Radiography", M. Arif and R. G. Downing (Eds), DES Tech Publications, Lancaster, PA, pp. 338–348 (2008).
21. T. A. Trabold, J. P. Owejan, D. L. Jacobson, M. Arif and P. R. Huffman, *Int. J. Heat Mass Transfer*, **49**, 4712 (2006).
22. A. Turhan, J. J. Kowal, K. Heller, J. Brenizer and M. M. Mench, *ECS Trans.*, **3**, 435 (2006a).
23. A. Turhan, K. Heller, J. S. Brenizer and M. M. Mench, *J. Power Sources*, **160**, 1195 (2006b).
24. A. Turhan, J. J. Kowal, K. Heller, L. Shi, J. Brenizer and M. M. Mench, 'Interaction of Design, Materials, and Interfacial Forces on Liquid Water Storage and Distribution in Polymer Electrolyte Fuel Cells', "Proceedings of the 8th World Conference on Neutron Radiography", Gaithersburg, MD, 2006c.
25. T. Ueda, N. Takenaka, H. Asano, K. Tanimoto, K.-I. Mochiki, Y. Kawabata and M. Matsubayashi, 'Visualization and Measurement of Dynamic Water Behavior in PEFC by Neutron Radiography', "Proceedings of the 8th World Conference on Neutron Radiography", Gaithersburg, MD, 2006 "Neutron Radiography", M. Arif and R. G. Downing (Eds), DES Tech Publications, Lancaster, PA, pp. 381–388 (2008).
26. K. Yoshizawa, K. Ikezoe, Y. Tasaki, D. Kramer, E. H. Lehmann and G. G. Scherer, *ECS Trans.*, **3**, 397 (2006).
27. J. Zhang, D. Kramer, R. Shimoi, Y. Ono, E. Lehmann, A. Wokaun, K. Shinohara and G. G. Scherer, *Electrochim. Acta*, **51**, 2715 (2006).
28. Y.-S. Chen, H. Peng, D. S. Hussey, D. L. Jacobson, D. T. Tran, T. Abdel-Baset and M. Biernacki, *J. Power Sources*, **170**, 376 (2007).
29. R. S. Fu, U. Pasaogullari, D. S. Hussey, D. L. Jacobson and M. Arif, *ECS Trans.*, **11**, 395 (2007).
30. D. S. Hussey, D. L. Jacobson, M. Arif, J. P. Owejan, J. J. Gagliardo and T. A. Trabold, *J. Power Sources*, **172**, 225 (2007).
31. I. Manke, Ch. Hartnig, M. Grünerbel, J. Kaczerowski, W. Lehnert, N. Kardjilov, A. Hilger, J. Banhart, W. Treimer and M. Strobl, *Appl. Phys. Lett.*, **90**, 184101 (2007).
32. R. Mukundan, J. R. Davey, T. Rockward, J. S. Spendlow, B. S. Pivovarov, D. S. Hussey, D. L. Jacobson, M. Arif and R. L. Borup, *ECS Trans.*, **11**, 411 (2007).

33. R. Mukundan, Y. S. Kim, T. Rockward, J. R. Davey, B. S. Pivovar, D. S. Hussey, D. L. Jacobson, M. Arif and R. L. Borup, *ECS Trans.*, **11**, 543 (2007).
34. J. P. Owejan, T. A. Trabold, J. J. Gagliardo, D. L. Jacobson, R. N. Carter, D. S. Hussey and M. Arif, *J. Power Sources*, **171**, 626 (2007).
35. J. P. Owejan, T. A. Trabold, D. L. Jacobson, M. Arif and S. G. Kandlikar, *Int. J. Hydrogen Energy*, **32**, 4489 (2007).
36. Ch. Hartnig, I. Manke, N. Kardjilov, A. Hilger, M. Grünerbel, J. Kaczerowski, J. Banhart and W. Lehnert, *J. Power Sources*, **176**, 452 (2008).
37. M. A. Hickner, N. P. Siegel, K. S. Chen, D. S. Hussey, D. L. Jacobson and M. Arif, *J. Electrochem. Soc.*, **155**, B294 (2008a).
38. M. A. Hickner, N. P. Siegel, K. S. Chen, D. S. Hussey, D. L. Jacobson and M. Arif, *J. Electrochem. Soc.*, **155**, B427 (2008b).
39. A. Turhan, K. Heller, J. S. Brenizer and M. M. Mench, *J. Power Sources*, **180**, 773 (2008).
40. T. Ueda, N. Takenaka, H. Asano, K. Tanimoto, K.-I. Mochiki, Y. Kawabata and M. Matsubayashi, *J. Power Energy Syst.*, **2**, 997 (2008).
41. J. P. Owejan, J. G. Gagliardo, J. M. Sergi and T. A. Trabold, 'Two-Phase Flow Considerations in PEMFC Design and Operation', "Proceedings of ASME ICNMM2008, 6th International Conference on Nanochannels, Microchannels and Minichannels", Paper ICNMM2008-62037, Darmstadt, June 22–25, 2008.
42. M. B. Chadwick, P. Obložinský, M. Herman, N. M. Greene, R. D. McKnight, D. L. Smith, P. G. Young, R. E. MacFarlane, G. M. Hale, S. C. Frankle, A. C. Kahler, T. Kawano, R. C. Little, D. G. Madland, P. Moller, R. D. Mosteller, P. R. Page, P. Talou, H. Trelleue, M. C. White, W. B. Wilson, R. Arcilla, C. L. Dunford, S. F. Mughabghab, B. Pritychenko, D. Rochman, A. A. Sonzogni, C. R. Lubitz, T. H. Trumbull, J. P. Weinman, D. A. Brown, D. E. Cullen, D. P. Heinrichs, D. P. McNabb, H. Derrien, M. E. Dunn, N. M. Larson, L. C. Leal, A. D. Carlson, R. C. Block, J. B. Briggs, E. T. Cheng, H. C. Huria, M. L. Zerkle, K. S. Kozier, A. Courcelle, V. Pronyaev and S. C. van der Marck, *Nucl. Data Sheet*, **107**, 2931 (2006).
43. D. S. Hussey, D. L. Jacobson, M. Arif, K. J. Coakley and D. F. Vecchia, 'In Situ Fuel Cell Water Metrology at the NIST Neutron Imaging Facility', "Proceedings of the ASME Fuel Cell Conference", New York, June 18–20, 2007.
44. U.S. Department of Energy, 'Hydrogen, Fuel Cells, and Infrastructure Technology Programs: Multi-Year Research, Development and Demonstration Plan', Section 3.4 – Fuel Cells, October 2007 <http://www1.eere.energy.gov/hydrogenandfuelcells/mypp/>.
45. S. Kandlikar, N. Rao, O. Lu, T. Trabold, J. Owejan and J. Allen, 'Visualization of Fuel Cell Water Transport and Performance Characterization Under Freezing Conditions', U.S. Department of Energy Hydrogen Program Review, ID# FCP22, May 16 (2007) http://www.hydrogen.energy.gov/annual_review07_fuelcells.html#p_transport.
46. E. H. Lehmann, G. Frei, G. Kuehne and P. Boillat, *Nucl. Instrum. Methods Phys. Res., Sect. A*, **576**, 389 (2007).
47. O. H. W. Siegmund, J. V. Vallerga, A. Martin, B. Feller, M. Arif, D. S. Hussey and D. L. Jacobson, *Nucl. Instrum. Methods Phys. Res., Sect. A*, **579**, 188 (2007).
48. W. B. Feller, P. L. White and P. B. White, 'Gamma Insensitive Highly Borated Microchannel Plates for Neutron Imaging', in "Neutron Radiography", M. Arif and R. G. Downing (Eds), DES Tech Publications, Lancaster, PA, pp. 583–591 (2008).
49. R. G. Downing, 'High Resolution Position Sensitive Neutron Detector (HRPSND)', in "Neutron Radiography", M. Arif and R. G. Downing (Eds), DES Tech Publications, Lancaster, PA, pp. 616–622 (2008).
50. J. S. Nico and W. M. Snow, *Annu. Rev. Nucl. Part. Sci.*, **55**, 27 (2005). Also, see http://en.wikipedia.org/wiki/Thermal_neutron. 2008.
51. B. E. Allman, P. J. McMahon, K. A. Nugent, D. Paganin, D. L. Jacobson, M. Arif and S. A. Werner, *Nature*, **408**, 158 (2000).
52. F. Pfeiffer, C. Grünzweig, O. Bunk, G. Frei, E. Lehmann and C. David, *Phys. Rev. Lett.*, **96**, 215505 (2006).
53. A. C. Kak and M. Slaney, 'Principles of Computerized Tomographic Imaging', Society of Industrial and Applied Mathematics (2001).
54. K. J. Coakley, D. S. Hussey and D. F. Vecchia, 'Statistical Learning Methods for Neutron Transmission Tomography of Fuel Cells', in "Neutron Radiography", M. Arif and R. G. Downing (Eds), DES Tech Publications, Lancaster, PA, pp. 155–164 (2008).